Face Image Super-resolution Reconstruction via Mapping Matrix and Multilayer Model

Yan Wang, Jianchun Wang, Fengju Li, Yancong Zhou, Min Xiong and Ming Li

Abstract—**Making full use of the information provided by the training set has always been the target of face image super-resolution reconstruction in the case of small samples. To solve the problem of full usage, we propose a novel algorithm via mapping matrix and multilayer model. Firstly, we double the training set by the flip method. Then, we extract one-step and two-step gradient features in the training set, and divide these face images and their feature images into many multi-scale patches. The reconstructed training set is formed by the patches which are in the same positions. We adopt high-resolution and low-resolution feature images simultaneously to build weights for the mapping matrix. To reduce local ghosting and blurring of the reconstructed image, the matrix constraint is constructed through processing the distance of different low-resolution and high-resolution feature image blocks. Last, the multilayer model is built by using image patches of different scales so that the reconstruction can reflect the degradation process of the image. The experimental results on the small sample database FERET, FEI and CAS-PEAL-R1 show that the proposed method can achieve better face image reconstruction quality compared with state-of-the-art methods.**

Index Terms—**Super-resolution reconstruction, Position patch, Non-local similarity, Mapping matrix**

I. Introduction

Nowadays, there are higher requirements for image quality in human-computer interaction. However, the images obtained in real scenes cannot meet the needs [1-3]. Super-resolution reconstruction is a cost-effective way to improve the quality of images, and widely applied in aerospace [4], the military [5] and biomedicine [6]. Super-resolution reconstruction algorithms of face images can be classified into two families of methods: (i) The multiple images based super-resolution [7-11], and (ii) The single image based super-resolution [12-23].

As the approaches based on multiple images need images taken continuously. The performance of super-resolution reconstruction will decrease if the information between the images is broken. The algorithms based on a single image have received a lot of attention in recent years owing to its wide application and good performance. Chang et al. [12] reconstructed a high-resolution image by using K neighbor image patches in the training set. However, such a method is prone to blur the reconstructed images. Timofte et al. [13] proposed an Anchored Neighborhood Regression (ANR) to improve the efficiency and accuracy of reconstruction. The method calculated the mapping matrix through a dictionary in the training stage. In the literature [14], the modified Fixed Neighborhood Anchored Regression (A+) was proposed. This method used the training set to construct the mapping matrix, and further improved the quality of the reconstructed image. Shi et al. [15] proposed to regularize the relationship between the target patch and the corresponding patch in the HR space and preserved local geometry in resolutions effectively. Huang et al. [16] reconstructed a low-resolution face image by sparse representation to solve the blurring problems at the cost of high time complexity [17].

As a typical single image based reconstruction algorithm, the patch-based method assumes patches at the same position in different face images having the same image structure. To make full use of this property, Ma et al. [18] constructed training set of patches at the same position to save the time of training dictionary, and thus enhanced the efficiency of reconstruction greatly. Farrugia et al. [19] built the linear models of the image patches by using the local geometric structure to avoid the uncertainty. Gao et al. [20] selected the specified patch for reconstructing face image by adding low-rank constraints to ensure the effectiveness of the training set and retain the details of the image. But the method does not satisfy the demands of high-quality images due to its reliance on the training set and ignoring the nature of the image. Gong et al. [21] enlarged the patches to a local window which enhanced the flexibility of reconstruction. Jiang et al. [22] proposed the algorithm of Locality -constrained Iterative Neighbor Embedding (LINE) to reconstruct the face image with the mapping relations in high-resolution image patches. The smooth regression updates the intermediate dictionary and enhances the detailed information of the image by smooth regression. However, the reconstructed images appear partial ghosting, blurring and some images even exist edge aliasing owning to the mapping matrix consisting only high-resolution image patches. Then in the literature [23], they proposed the Smooth Regression with Local Structure Prior (SRLSP) to construct a weight matrix to achieve smooth regression.

In order to solve these problems, we propose a face image

Manuscript received July 15, 2019; revised November 14, 2019. This work was supported by Tianjin Sci-tech Planning Projects (No. 18ZXZYNC00170), Technical Expert Project of Tianjin (No. 19JCTPJC55000).

Yan Wang and Yancong Zhou is with the College of Information Engineering, Tianjin University of Commerce, Tianjin 300134, China (corresponding author, e-mail: zycong78@126.com).

Jianchun Wang and Fengju Li are with Agriculture Information Department, Tianjin Academy of Agricultural Sciences, Tianjin 300192, China.(corresponding author, e-mail: wangmiao115@126.com; lfj_51083@sina.com).

Min Xiong is with the School of Information, Hebei University of Technology, Tianjin 300401, China (e-mail: 106748693@ qq.com).

Ming Li is with Tianjin Zhongwei Aerospace Data System Technology Company, Tianjin 300301, China (email:Mingli@163.com)

super-resolution reconstruction algorithm via a mapping matrix and multilayer model. The novelty and contribution of our work are as follows:

(1) The training set is optimized. The features of first-step gradient and second-step gradient are extracted from the preprocessed images in training set. Then the images and their corresponding feature images are divided into many patches. The similar patches of the reconstructed patch are searched according to the non-local similarity of the low resolution feature images. Finally, the optimized training set consisted of patches is obtained.

(2) A weight mapping matrix is proposed. The matrix can reduce local ghosting and blurring of the reconstructed image effectively. Meanwhile, the constraints of weight matrix reduce local ghosting of the reconstructed images.

(3) Multilayer model is constructed by using different scale of patches. The model can reflect the degradation process of a reconstructed face image.

The rest of the paper is organized as follows: Section II introduces the proposed method. Section III discusses the experimental results. The paper is concluded in Section IV.

II. Proposed Method

A. Preprocess

(1) Training set preprocessing

The images in the training set are flipped left and right according to the bilateral symmetry property of face image. The low-resolution training set P_l and high-resolution training set P_h are obtained as formula (1) and (2).

$$P_l = [p_l^1, p_l^2, ..., p_l^M] \tag{1}$$

$$P_h = [p_h^1, p_h^2, ..., p_h^M] \tag{2}$$

where M is the number of images.

We extract first-step and second-step gradient feature of all images in training set to obtain feature sets G_l and G_h:

$$G_l = [g_l^1, g_l^2, ..., g_l^M] \tag{3}$$

$$G_h = [g_h^1, g_h^2, ..., g_h^M] \tag{4}$$

The processing procedure of the training set is：

a). Each image of the high-resolution image set P_h and its corresponding feature image set G_h is blocked with overlapping to patches. The size of every patch is $R*R$ pixels. The overlapping mode is that the current patch overlaps K rows of pixels with the upper and lower adjacent patches respectively, and overlaps K columns of pixels with left and right adjacent patches respectively, $0 \le K \le R/2$.

b). The patches of each image in P_h and G_h are coded from top to bottom, from left to right, numbered1,2,…, U,. The patch at the same position has the same number.

c). The same overlapped block is performed on each image of the low-resolution set P_l and its corresponding feature image set G_l. The patch size is $(R/d)*(R/d)$ pixels, where d is the multiple of reduction. The current patch overlaps k/d rows of pixels with the upper and lower adjacent patch, and overlaps k/d columns of pixels with the left and right adjacent patch. The coding of patches is the same as step b).

d). All patches in P_l and G_l are coded from top to bottom, from left to right, numbered1,2,…, U, and the same number represent the image patch at the same position.

(2) Testing set preprocessing

The processing procedure of testing set is:

a). The low-resolution image I_{tl} in the testing set is amplified by the bi-resolution interpolation [26] to obtain the enlarged image I_{th}. Therefore, I_{th} has the same size with the high-resolution image.

b). The corresponding feature images g_{tl} and g_{th} can be obtained by extracting first-step and second-step gradient features of I_{tl} and I_{th} respectively.

c). The overlapping patch performed on I_{th} , g_{th} , I_{tl} and g_{tl} is the same as which on P_h, G_h, P_l, and G_l.

B. Optimizing Datasets

In a face image, there are many regions with similar structural and texture information. This property is called image non-local similarity [25, 27]. With this aspect, a similar patch of the *jth* image patch can be found in a feature image.

The process of searching for the similar patch of the *jth* feature image patch $g_{tl,j}$ is:

All patches in feature image g_{tl} are scanned from top to bottom, from left to right. The Euclidean distance between the scanned feature images patches and $g_{tl,j}$ is calculated. Then, all patches are sorted in an ascending order according to the distance. Taking the first n patches as the similar patches of $g_{tl,j}$, and the set of similar patches is denoted as $[v_1, v_2, \ldots, v_n]$.

The *jth* patch and the $[v_1, v_2, \ldots, v_n]$ patches in G_l constitute $G_{l,j}$:

$$G_{l,j} = [g_{l,j}^1, g_{l,v_1}^1, g_{l,v_2}^1, ..., g_{l,v_n}^1, ..., g_{l,j}^M, g_{l,v_1}^M, g_{l,v_2}^M, ..., g_{l,v_n}^M] \tag{5}$$

$G_{l,j}$ can also be represented as formula (6):

$$G_{l,j} = \left[g_{l,j1}, g_{l,j2}, ..., g_{l,jM*(1+n)} \right] \tag{6}$$

where M is the number of feature images, and each image have $(1+n)$ patches.

The *jth* patch and the $[v_1, v_2, \ldots, v_n]$ patches in G_h constitute $G_{h,j}$:

$$G_{h,j} = \left[g_{h,j1}, g_{h,j2}, ..., g_{h,jM*(1+n)} \right] \tag{7}$$

The *jth* patch and the $[v_1, v_2, \ldots, v_n]$ patches in P_l constitute $P_{l,j}$:

$$P_{l,j} = \left[p_{l,j1}, p_{l,j2}, ..., p_{l,jM*(1+n)} \right] \tag{8}$$

The *jth* patch and the $[v_1, v_2, \ldots, v_n]$ patches in P_h constitute $P_{h,j}$:

$$P_{h,j} = \left[p_{h,j1}, p_{h,j2}, ..., p_{h,jM*(1+n)} \right] \tag{9}$$

C. Mapping Matrix

The existing patch-based reconstruction algorithms work as follows: calculating the mapping relations among low-resolution image patches, and mapping the same relationship to the high-resolution image patch to obtain the reconstructed patch. However, low-resolution image patches cannot fully represent high-resolution image patches. Therefore, we uses both of the low-resolution feature image patches and high-resolution feature image patches to construct the constraints. Then, the mapping matrix is obtained by these constraints to reconstruct high-resolution image.

The process of calculating the mapping matrix is:

a). Calculating the Euclidean distance $dist\_g_{tl,j}\_G_{l,j}$ between $g_{tl,j}$ and all of the feature patches in $G_{l,j}$ as (10):

$$dist\_g_{tl,j}\_G_{l,j} = [dist(g_{tl,j}, g_{l,j1}), dist(g_{tl,j}, g_{l,j2}), ..., dist(g_{tl,j}, g_{l,jM*(1+n)})] \quad (10)$$

b). Calculating the Euclidean distance $dist\_g_{th,j}\_G_{h,j}$ between $g_{th,j}$ and all of the feature patches in $G_{h,j}$ as (11):

$$dist\_g_{th,j}\_G_{h,j} = [dist(g_{th,j}, g_{h,j1}), dist(g_{th,j}, g_{h,j2}), ..., dist(g_{th,j}, g_{h,jM*(1+n)})] \quad (11)$$

c). Calculating the weight matrix W_j of the *jth* patch as:

$$W_j = \begin{bmatrix} \frac{1}{(dist(g_{tl,j}, g_{l,j1}) + dist(g_{th,j}, g_{h,j1}))^{\alpha}} & & 0 \\ & \ddots & \\ 0 & & \frac{1}{(dist(g_{tl,j}, g_{l,jM*(1+n)}) + dist(g_{th,j}, g_{h,jM*(1+n)}))^{\alpha}} \end{bmatrix} \quad (12)$$

where α is the smoothing factor.

d). A linear mapping relation between the *jth* high-resolution image patch and its corresponding low-resolution image patch can be got by formula (13):

$$P_{h,j} = A_j^{\mathrm{T}} P_{l,j} \quad (13)$$

where A_j^{T} is the mapping matrix of the *jth* image patch, T is the transpose of the matrix.

e). The optimal mapping matrix can be calculated as:

$$A_j^{'} = \min_{A_j} \| P_{h,j} - A_j^{\mathrm{T}} P_{l,j} \| \quad (14)$$

f). (14) can be further constrained as:

$$A_j^{''} = \min_{A_j} \| P_{h,j} - A_j^{\mathrm{T}} P_{l,j} \|_{W_j} \quad (15)$$

where $\| Z \|_{W_j} = tr(ZW_jZ^{\mathrm{T}})$, $tr(.)$ is the trace of matrix.

g). We add a regularization term to smooth the mapping process as formula (16):

$$A_j^{*} = \min_{A_j} \| P_{h,j} - A_j^{\mathrm{T}} P_{l,j} \|_{W_j} + \lambda \| A_j \|_F^2 \quad (16)$$

where $\| Z \|_F^2 = tr(ZZ)$, F is the Frobenius norm.

h). The mapping matrix of the *jth* patch can be obtained as:

$$A_j^{*} = (P_{l,j} W_j P_{l,j}^{T} + \lambda E)^{-1} P_{h,j} W_j P_{l,j}^{T} \quad (17)$$

where E is the unit matrix.

With $(A_j^{*\mathrm{T}} * I_{tl,j}^{\mathrm{T}})^{\mathrm{T}}$, we can get the high-frequency information of the reconstructed patch. The reconstructed high-resolution patch $I_{th,j}^{'}$ can be obtained by interpolating the high-frequency information into $I_{tl,j}$ according to the method of [24].

D. Multilayer Model

The multilayer model is constructed as follows:

To obtain a low-resolution image $I_{tl,j}^{'}$, the corresponding high-resolution image $I_{th,j}^{'}$ obtained in steps *A-C* is dimensionally reduced by nearest neighbor interpolation [30].

The *ith* low-resolution image p_l^i can be reconstructed as:

a). Training set is composed by $[p_l^1, p_l^2, ..., p_l^{i-1}, p_l^{i+1}, ..., p_l^N]$ and $[p_h^1, p_h^2, ..., p_h^{i-1}, p_h^{i+1}, ..., p_h^N]$. p_l^i is reconstructed according to *A-C* steps to obtain the high-resolution face image $p_h^{i'}, i = 1, 2, ...M$.

b). The dimension of $p_h^{i'}$ is reduced by the nearest neighbor interpolation to obtain $p_l^{i'}, i = 1, 2, ...M$.

c). All the images are segmented into patches. The patch size of high-resolution face images is $R_2 * R_2$ pixels, $2 \le R_2 \le 16$, and the overlapping size between the adjacent patches is K_2. The patch size of low-resolution face images is $R_2 / d \ * R_2 / d$ pixels, and the overlapping size between the adjacent patches is K_2 / d.

d). Super-resolution reconstruction is performed again to obtain the final reconstructed face image.

III. Experiments

We compare the proposed method with the ANR [13], A+ [14], LINE [22], SRLSP [23], Bicubic [24] on FERET, FEI and CAS-PEAL-R1 database. To obtain a low-resolution image, the nearest neighbor interpolation method is used to reduce the image size by two times. So the image size of the FERET is reduced from 80*80 pixels to 40*40 pixels, the image size of the FEI is reduced from 80*100 pixels to 40*50 pixels, and the image size of the CAS-PEAL-R1 is reduced from 100*100 pixels to 50*50 pixels.

A. Parameter Setting

We select 100 images as the training set, 50 images as the testing set randomly in the FERET database.

Table I shows the PSNR (Peak Signal to Noise Ratio) and SSIM (Structural Similarity Index) value in different expanding modes. NE means no expanding, FLR and FUD represent flip left and right and flip up and down respectively, and R denote rotate. The result suggest that the expanding mode of flipping left and right (FLR) can get the highest PSNR and SSIM. In this paper, we double the training set by this mode.

There are two criteria for feature selection: the one is that the features contain as much valid information as possible; the other is that the feature can maintain the structure consistency of the high-resolution patch and low-resolution patch. Different feature combinations can influence the result.

Table II shows the average PSNR and SSIM obtained by different feature combinations.

TABLE I
PSNR(dB) and Ssim with Different Expansion Modes

	NE	FLR	FUD	R90°	R180°	R270°
PSNR	30.41	**30.72**	30.53	30.47	30.51	30.51
SSIM	0.9040	**0.9115**	0.9050	0.9054	0.9050	0.9059

TABLE II
PSNR(dB) and Ssim with Different Feature Combinations

	FSG + Pixel	FSG + SSG	SSG + Kirsch	SSG + LBP	SSG + Haar
PSNR	30.79	**30.89**	30.78	30.82	30.88
SSIM	0.9126	**0.9150**	0.9133	0.9135	0.9149

It can be seen in Table II that the average PSNR and SSIM can get the highest value when applying first-step and second-step gradient features. Therefore, this paper selects both first-step gradient (FSG) and second- step gradient (SSG) as the features of the face image.

Different number of similar patch is selected to obtain the average PSNR and SSIM, as shown in Fig.1.

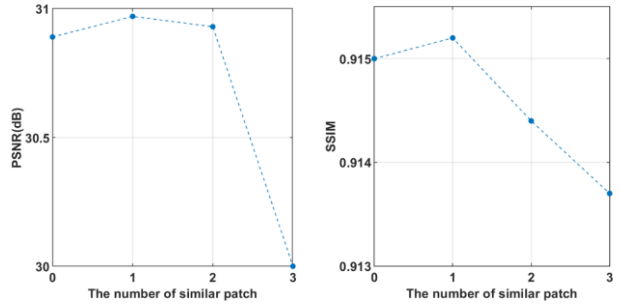

Fig.1. The PSNR and SSIM of the proposed method using different number of similar patch on FERET dataset

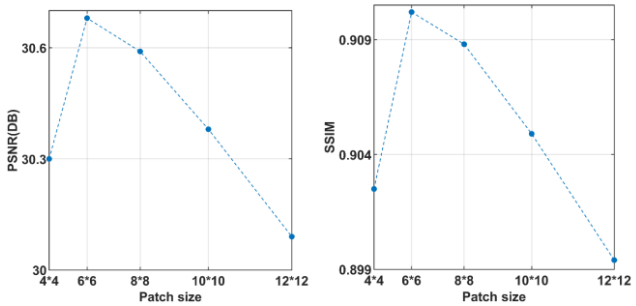

Fig.2. The PSNR and SSIM of the proposed method using different patch size on FERET dataset

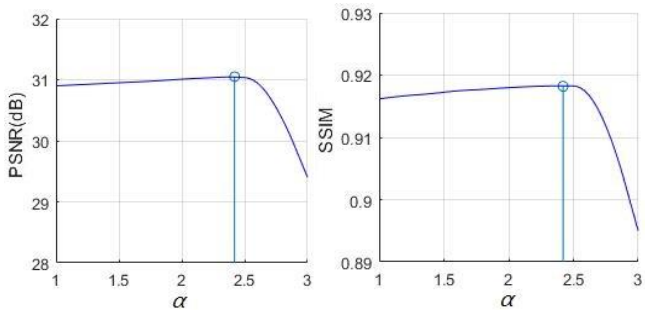

Fig. 3. The PSNR and SSIM change with various smooth factor α.

It can be seen that as the number of similar patch is 1, the average PSNR and SSIM can reach the highest value. With the increase of the number, the average value of PSNR and SSIM gradually decrease.

In Fig.2 different high-resolution patch sizes lead to different reconstruction results. The corresponding low-resolution patch size can be got by reducing proper multiples of high-resolution patch.

Fig.2 suggests that PSNR and SSIM can reach the highest value when the patch size is 6*6. Therefore, the proposed method uses 6*6 patch size for image reconstruction.

We adopt factor α to smooth the constraint of the mapping matrix. An experiment is performed to select the best α value, the other parameters are set as above experiments. Fig. 4 shows the average PSNR and SSIM change with various α.

It suggests that the value gradually increases with the value of α gradually increasing from 0. When α is 2.4, the average PSNR and SSIM values reach their peak value, which are 31.14dB and 0.9174dB, respectively. As α continues to increase, the average PSNR and SSIM gradually decrease. Thus, the value of α in this paper is set as 2.4

B. Comparison with Other Methods

In the experiments, we set optimal parameters for every algorithm and use the same training and testing set.

The ANR algorithm takes a dictionary size of 1024 and a neighborhood size of 40; the A+ algorithm takes a dictionary size of 1024, the neighborhood size is 2048, the number of image patches in training set is 5000000; the LINE algorithm takes a neighborhood size of 150; the patch size of SRLSP algorithm is 8*8 pixels and the smoothing factor is 1.2. Since the image size reconstructed by ANR and A+ is different from others, we adopt Bicubic algorithm to enlarge the image, and then pad the edge of the enlarged image into the reconstructing image of ANR and A+.

In addition to PSNR and SSIM, we also introduce the third image quality assessment model FSIM (Feature Similarity) to evaluate the results of different methods [29].

(1) Experiments on FERET Database

We select 100 images randomly as the training set and 50 images as a testing set on the FERET database.

Fig. 4 shows the reconstruction result of five images. It can be seen from the results that the image obtained by the Bicubic is the most blurred, especially in the eyes, nose and mouth. Compared with Bicubic, the image blurring phenomenon reconstructed by ANR and A+ is reduced. However, the details of the image are not clear enough due to excessive smoothing, and the local structural features on the eyes, nose and mouth are not obvious. The details reconstructed by LINE and SRLSP are better restored, and the local features are more obvious. However, there are local ghosting or blurring in the nose and mouth, and edge aliasing in some images. Our method not only overcomes the blurring of the image, but also avoids the local ghosting and edge aliasing, obtain the optimal reconstructed image.

The experimental results of PSNR, SSIM and FSIM on the FERET database are shown in Table III. The performance of average PSNR, SSIM and FSIM is better than the Bicubic, ANR, A+, LINE, and SRLSP algorithms.

(2) Experiments on FEI database

On the FEI database, 150 images are randomly selected as the training set, 50 images as the testing set. Fig. 5 shows the reconstruction result of five images.

From left to right, there are images reconstructed by Bicubic, ANR, A+, LINE, SRLSP, our proposed method and the original image. It can be seen from the results that the image obtained by the Bicubic method is the most blurred. The image reconstructed by ANR and A+ is more obvious, the details of the eyes, mouth and mustache are blurred due to their excessive smoothing. The details of the image reconstructed by LINE and SRLSP method are better restored. But the local regions of the mouth are blurred. The proposed method gets the best result and overcomes the shortcomings of blurring and local ghosting.

Table IV shows the average PSNR, SSIM and FSIM values obtained by different methods. It can be seen that the average PSNR, SSIM and FSIM of proposed algorithm are better than other state-of-the-art algorithms. The average value of PSNR,

SSIM and FSIM is higher than the Bicubic, ANR, A+, LINE, and SRLSP algorithms.

(3) Experiments on CAS-PEAL-R1 database

The experiments on the CAS-PEAL-R1 database are shown in Fig. 6, in which 300 images are randomly selected as the training set and 100 images as the testing set. It is Bicubic, ANR, A+, LINE, SRLSP, the image reconstructed by the algorithm and the original image from left to right.

It can be seen from the results that the image obtained by the Bicubic is the most blurred. The details of the image reconstructed by LINE and SRLSP are better restored. Especially the details of the eyes, mouth and nose, but some local regions are blurred due to excessive smoothing. However, there still exist local ghosting in some regions of eyes and mouth. The proposed method get the best result yet.

Table V shows the average PSNR, SSIM and FSIM values obtained by different algorithms. It can be seen that the average PSNR, SSIM and FSIM of proposed algorithm are better than other algorithms.

TABLE III
PSNR AND SSIM WITH DIFFERENT METHODS ON FERET

Methods	PSNR(dB)	SSIM	FSIM
Bicubic[26]	27.95	0.8521	0.8550
ANR[15]	29.81	0.9026	0.9133
A+[16]	30.05	0.9102	0.9220
LINE[24]	29.51	0.8841	0.9052
SRLSP[25]	30.48	0.9056	0.9214
Ours	31.07	0.9173	0.9368

TABLE IV
PSNR AND SSIM WITH DIFFERENT METHODS ON FEI

Methods	PSNR(dB)	SSIM	FSIM
Bicubic[26]	27.64	0.9278	0.8779
ANR[15]	32.27	0.9713	0.9485
A+[16]	35.51	0.9736	0.9561
LINE[24]	33.93	0.9702	0.9372
SRLSP[25]	34.90	0.9755	0.9534
Ours	35.61	0.9791	0.9618

TABLE V
PSNR AND SSIM WITH DIFFERENT METHODS ON CAS-PEAL-R1

Methods	PSNR(dB)	SSIM	FSIM
Bicubic[26]	29.27	0.9364	0.9451
ANR[15]	35.07	0.9740	0.9583
A+[16]	35.62	0.9761	0.9675
LINE[24]	34.67	0.9724	0.9500
SRLSP[25]	35.19	0.9748	0.9611
Ours	35.67	0.9774	0.9824

(4) Application of face recognition

Face recognition is one of the applications of face image super-resolution reconstruction. We conduct a face recognition process to evaluate the effect of the proposed method through an improved LBP [30] which is an effective face recognition algorithm. Firstly, the original images in FERET database are super-resolution reconstructed by the method of Bicubic, ANR, A+, LINE, SRLSP and the proposed method respectively. A total of 6500 images of 450 persons are selected for experiments. Then, we introduce the improved LBP to extract the features of images. Finally, KNN(K Nearest Neighbor) is applied for classification and the face can be recognized. The results (recognition rate) are showed in Table VI. As we can see, the proposed method shows superior performance than other algorithms in the application of recognizing face images.

TABLE VI
FACE RECOGNITION OF DIFFERENT METHODS ON FEI DATABASE

Methods	Recognition Rate (%)
Bicubic[26]	56.9
ANR[15]	85.7
A+[16]	88.3
LINE[24]	86.2
SRLSP[25]	87.9
Ours	91.3
Original images	95.4

IV. CONCLUSIONS

This paper proposes a face multilayer super-resolution reconstruction algorithm via mapping matrix and multilayer model. The problem of lacking data is handled through a series of face image preprocessing. At the same time, the matrix constraints to achieving smooth regression calculation overcome the shortcoming of the traditional algorithms only considering the mapping relationship between low-resolution image patches. Image reconstruction can better reflect the image degradation process by establishing a multilayer model. The edge saw-tooth, local ghost and blurring of the reconstructed image are greatly reduced. The experimental results on the FERET, FEI and CAS-PEAL-R1 database show that the proposed algorithm can achieve better results.

However, this paper is based on the fact that different face images have the same structure at the same position, which requires strict alignment of the face image. Therefore, the future work is how to strictly align two different face images to ensure the similarity of patches in the same position.

REFERENCES

[1] F. Liang, Y. Xu, M. Zhang, L. Y. Zhang. “A POCS algorithm based on text features for the reconstruction of document images at super-resolution,” Symmetry, vol.8, no. 10, pp.102-116, 2016.

[2] Y. Li, F. Xu, F. Zhang, P. Y. Xu, M. S. Zhang, M. Fan. “DLBI: deep learning guided Bayesian inference for structure reconstruction of super-resolution fluorescence microscopy,” Bioinformatics, 2018, vol. 34, no.13, pp.284-294.

[3] Y. G. Zhang; M, J. M. “Single image super-resolution by non-linear sparse representation and support vector regression,” Symmetry, vol.9, no. 2, pp.24-38, 2017.

[4] A.Xiao, Z. Wang, L.Wang, Y. Ren. “Super-resolution for "Jilin-1" satellite video imagery via a convolutional network,” Sensors, vol.18, no.4, pp.1194-1203, 2018.

[5] L. Yue, H. Shen, J. Li, Q.Yan, H. Zhang, L. Zhang. “Image Super-resolution: The techniques, Applications, and Future,” Signal Process, vol.128, pp. 389-408, 2016.

[6] S. Jian, D. M. Sima,S. N.Faezeh, G. Hangel, W. Bogner, S. Williams, S. V. Huffel, F. Maes, D. Smeets. “Patch-Based super-resolution of MR spectroscopic images: application to multiple sclerosis,” Frontiers in Neuroscience. no.11, pp.1-12, 2017.

[7] A. Kappeler, S. Yoo, Q. Dai, A. K. Katsaggelos. “Video Super-Resolution with convolutional neural networks,” IEEE Transactions on Computational Imaging, vol.2, no.2, pp.109-122, 2016.

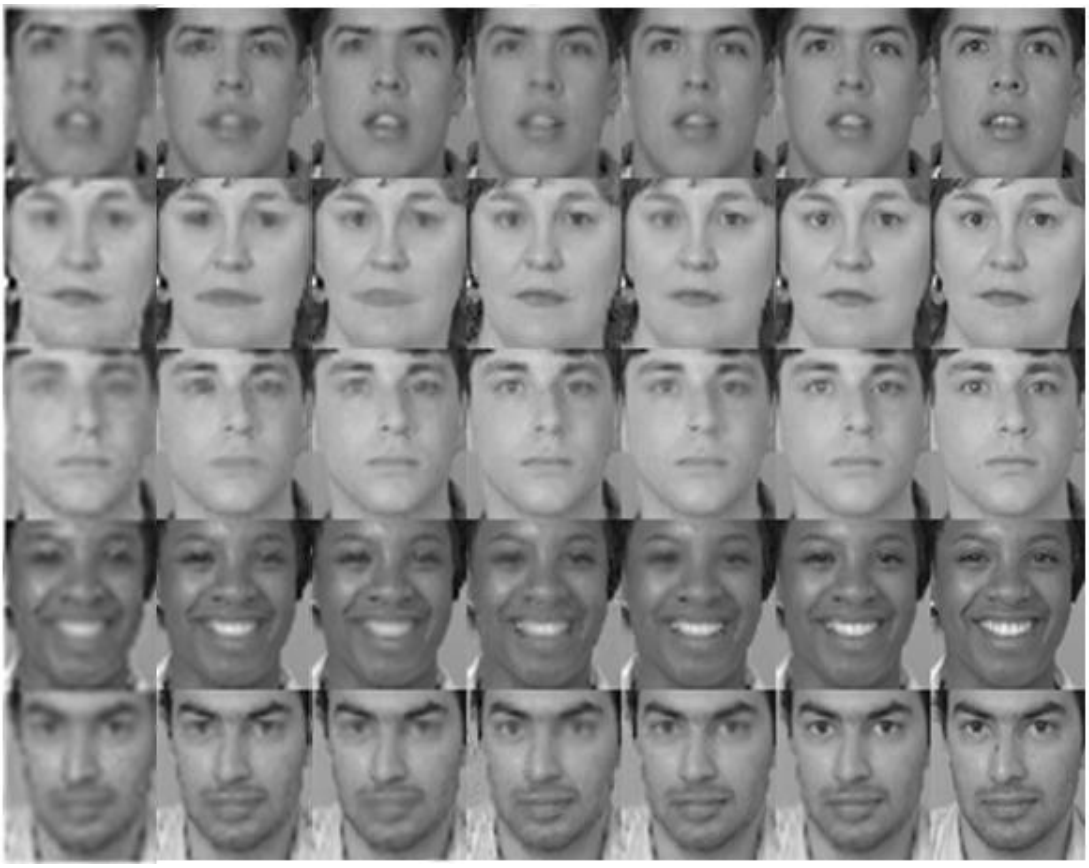

(a) (b) (c) (d) (e) (f) (g)

Fig. 4. Comparisons of super-resolution reconstruction results based on different methods on the FERET face database. (a) The Bicubic method [24]. (b) The ANR method [13]. (c) The A+ method [14]. (d) The LINE method [22]. (e) The SRLSP method [23]. (f) Our method. (g) The original face images.

(a) (b) (c) (d) (e) (f) (g)

Fig. 5. Comparisons of super-resolution reconstruction results based on different methods on the FEI face database. (a) The Bicubic method [24]. (b) The ANR method [13]. (c) The A+ method [14]. (d) The LINE method [22]. (e) The SRLSP method [23]. (f) Our method. (g) The original face images

(a) (b) (c) (d) (e) (f) (g)

Fig. 6. Comparisons of super-resolution reconstruction results based on different methods on the CAS-PEAL-R1 face database. (a) The Bicubic method [24]. (b) The ANR method [13]. (c) The A+ method [14]. (d) The LINE method [22]. (e) The SRLSP method [23]. (f) Our method. (g) The original face images.

[8] Z. H. Wu, M. J. Sun, Z. S. Gu, M. Y. Fan. "Second-Order directional total generalized variation regularization for image super-resolution," Chinese Journal of Electronics, vol.45, no.11, pp.59 – 66, 2017 .

[9] A. Laghrib, A. Hakim, S. Raghay, M. E. Rgabi. "A robust multi-frame super resolution based on curvature registration and second order vibrational regularization," International Journal of Tomography & Simulation, vol.28, no. 2, pp. 63-71, 2015.

[10] I. E. Mourabit, M. E. Rhabi, A. Hakim, A. Laghrib, E. "Moreau. A new denoising model for multi-frame super-resolution image reconstruction," Signal Processing, vol.132, pp. 51-65, 2017.

[11] Q. X. Lai, Y. W. Nie, Z. S. Zhang, H. Q. Sun. "Temporal coherent video super-resolution via pre-frame-constrained sparse reconstruction," Proceedings of Computer Graphics International, 2018, pp. 223-232.

[12] H. Chang, D. Y. Yeung, Y. Xiong. "Super-Resolution through neighbor embedding," IEEE Computer Society Conference on Computer Vision and Pattern Recognition, 2004, pp: 275-282.

[13] R. Timofte, V. De, L. V. Gool. "Anchored neighborhood regression for fast example-based super-resolution," IEEE International Conference on Computer Vision, 2013, pp. 1920-1927.

[14] R. Timofte, V. D. Smet, L. V. Gool. "A+: Adjusted anchored neighborhood regression for fast super-resolution," Asian Conference on Computer Vision, 2014, pp. 111-126.

[15] J. Shi, X. Liu, Y. Zong, C. Qi, G. Zhao. "Hallucinating Face Image by Regularization Models in High-Resolution Feature Space," IEEE Transactions on Image Processing, vol. 27, no.6, pp. 2980-2995, 2018.

[16] K.Huang, R. Hu, J. Jiang, Z. Han, F. Wang. "HRM Graph Constrained Dictionary Learning for Face Image Super-resolution," Multimedia Tools &Application, vol.76, no.2, pp. 3139-3162, 2017.

[17] Y. Xiao, J. Z. Wu, and W. Gao. "Fuse and Divide Technologies for Sparse Vector Learning in Ontology Algorithms," Engineering Letters, vol. 24, no.3, pp.307-316, 2016

[18] X. Ma, J. Zhang, C. Qi. "Hallucinating face by position-patch," Pattern Recognition, vol.43, no.6, pp. 2224-2236, 2010.

[19] R. A. Farrugia, C. Guillemot. "Face hallucination using linear models of coupled sparse support," IEEE Transactions on Image Processings, no. 26, pp. 4562-4577, 2017.

[20] G. W. Gao, X. Y. Jing, P. Huang, Q. Zhou, S. S. Wu, D. "Yue. Locality-Constrained double low-rank representation for effective face hallucination," IEEE Access, vol. 4, no.99, pp.8775-8786, 2017.

[21] M. Gong, K. Wang. "Single face hallucination via local neighbor patches," International Journal of Electronics Communications, vol.74, pp.88-93, 2017.

[22] J. Jiang, R. Hu, Z. Wang, Z. Han. "Face super-resolution via multilayer locality-constrained iterative neighbor embedding and intermediate dictionary learning," IEEE Transactions on Image Processing, vol. 23, no.10, pp. 4220-4231, 2014.

[23] J. Jiang, C. Chen, J.Y. Ma, Z. Wang, Z. Y. Wang, R. M. Hu. "SRLSP: A face image super-resolution algorithm using smooth regression with local structure prior," IEEE Transactions on Multimedia, vol.19, no.1, pp.27-40, 2017.

[24] X. Li, M. T. Orchard. "New edge-directed interpolation," IEEE Transactions on Image Processing, vol.10, no.10, pp. 1521-1527, 2001.

[25] Z. J, Huang, C. Y. TANG, Y. T. Chen, Q. Li. "Remote sensing image reconstruction based on nonlocal similarity and low rank matrix," *Acta Optica Sinica*. vol.6, pp. 97-107, 2016.

[26] Ghosh, Debdas, D. Ghosh. "Cubic Interpolation: A line search technique for fuzzy optimization problems," International Journal of Applied and Computational Mathematics, vol. 4, no. 1, pp.23-29, 2018.

[27] Y. F. Chen, H. X. Gao, Z. L. Wu, H. Kang. "An adaptive image sparse reconstruction method combined with nonlocal similarity and cosparsity for mixed Gaussian-Poisson noise removal," Optoelectronics Letters, vol.14, no.1, pp.57-60, 2018.

[28] J, Aïzan. E. C. Ezin, C. A. Motamed. "Face Recognition Approach Based on Nearest Neighbor Interpolation and Local Binary Pattern," Signal-image Technology & Internet-based Systems, 2017, pp.76-81.

[29] L.Zhang, X.Mou, D.Zhang. "A feature similarity index for image quality assessment," IEEE Transactions on Image Processing, vol.20, no.8, pp.2378-2386, 2011.

[30] D. Chen, X. Cao, F. Wen. "Blessing of dimensionality: High-dimensional feature and its efficient compression for face verification," IEEE Conference on Computer Vision and Pattern Recognition, 2013, pp. 3025-3032.